Valence and magnetic ordering in intermediate valence compounds: TmSe versus SmB_6

2006 J. Phys.: Condens. Matter 18 2089

(http://iopscience.iop.org/0953-8984/18/6/021)

INSTITUTE OF PHYSICS PUBLISHING JOURNAL OF PHYSICS: CONDENSED MATTER

J. Phys.: Condens. Matter **18** (2006) 2089–2106 doi:10.1088/0953-8984/18/6/021

Valence and magnetic ordering in intermediate valence compounds: TmSe versus SmB_6

J Derr, G Knebel, G Lapertot, B Salce, M-A Méasson and J Flouquet

Département de Recherche Fondamentale sur la Matière Condensée, CEA Grenoble, 17 rue des Martyrs, 38054 Grenoble Cedex 9, France

E-mail: julien.derr@cea.fr

Received 13 October 2005, in final form 10 January 2006
Published 27 January 2006
Online at stacks.iop.org/JPhysCM/18/2089

Abstract

The intermediate valence systems TmSe and SmB_6 have been investigated up to 16 and 18 GPa by ac microcalorimetry with a pressure (p) tuning realized *in situ* at low temperature. For TmSe, the transition from an antiferromagnetic insulator for $p < 3$ GPa to an antiferromagnetic metal at higher pressure has been confirmed. A drastic change in the p variation of the Néel temperature (T_N) is observed at 3 GPa. In the metallic phase ($p > 3$ GPa), T_N is found to increase linearly with p. A similar linear p increase of T_N is observed for the quasitrivalent compound TmS, which is at ambient pressure equivalent to TmSe at $p \sim 7$ GPa. In the case of SmB_6 long range magnetism has been detected above $p \sim 8$ GPa, i.e. at a pressure slightly higher than the pressure of the insulator to metal transition. However a homogeneous magnetic phase occurs only above 10 GPa. The magnetic and electronic properties are related to the renormalization of the 4f wavefunction either to the divalent or the trivalent configurations. As observed in SmS, long range magnetism in SmB_6 occurs already far below the pressure where a trivalent Sm^{3+} state will be reached. It seems possible to describe roughly the physical properties of the intermediate valence equilibrium by assuming formulae for the Kondo lattice temperature depending on the valence configuration. Comparison is also made with the appearance of long range magnetism in cerium and ytterbium heavy fermion compounds.

1. Introduction

Recently, a major interest was the study of the high pressure phase diagrams of heavy fermion compounds (HFCs) [1]. However, in these systems, the departure from the trivalent configuration is weak; the occupation number n_f of the $4f^1$ configuration is nearly one. Unusual magnetic properties found notably on ytterbium HFC such as $YbRh_2Si_2$ [2, 3] push to revisit other situations with magnetic and valence fluctuations occurring between two 4f

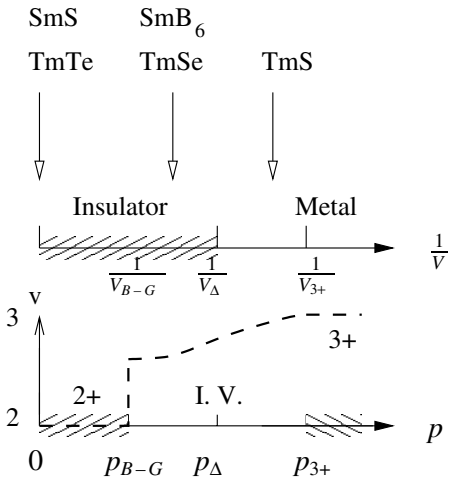

Figure 1. Valence state, as a function of the density, i.e. the inverse of the molar volume V. For $V < V_{\mathrm{B-G}}$, the system jumps from 2+ black (B) phase to IV gold (G) phase. Up to $V_{\mathrm{B-G}} > V > V_\Delta$ the system is still insulating (the dashed lines represent the insulating character). Magnetism also looks governed by the 2+ configuration. For $V < V_\Delta$, the system is metallic, and magnetism looks governed by the 3+ configuration. The trivalent limit will appear for $V_{3+} < V_\Delta$. Long range magnetism in SmS and SmB_6 appear for $\frac{1}{V} \sim \frac{1}{V_\Delta} + \epsilon < \frac{1}{V_{3+}}$. Of course it always occurs for TmSe whatever is the valence.

configurations. The cases of intermediate valence compounds (IVCs) such as SmS, SmB_6 and TmSe, are particularly interesting [4].

To characterize the intermediate valent state, a key parameter is the occupation number n_f of the trivalent configuration linked to the valence v by $v = 2 + n_f$ when the valence fluctuation occurs between the divalent and the trivalent state (case of Sm, Tm and Yb) or $v = 4 - n_f$ when it happens between the trivalent and tetravalent state (case of Ce). The important difference between Sm, Tm or Yb compounds is that n_f can vary from 0 to 1 while in Ce intermetallic compounds: $n_f > 0.8$ and at least long range magnetic ordering (M) occurs only for $n_f > 0.9$ [5]. TmSe [6–9] as well as SmS [4] and SmB_6 [10] in their low pressure intermediate valent gold phase have a valence near 2.6–2.7. Their trivalent limit will be reached smoothly only at very high pressure above 10 GPa for TmSe and 20 GPa for SmS and SmB_6 [11–13]. As will be discussed, the striking point is that for these three systems the change from insulating to metallic conduction at low temperature occurs when $n_f \sim 0.8$.

The valence mixing between the divalent (2+) and trivalent (3+) configurations of the rare earth (RE) ions is associated with the release of an itinerant 5d electron according to the relation $RE^{2+} \Longleftrightarrow RE^{3+} + e^-5d$. Experimentally, the effect of pressure is to broaden the bands and move this equilibrium to the right (increasing n_f). Of course, band structure calculations are necessary to describe the real situation, but the chemical equilibrium is worthwhile to consider. In the divalent black (B) phase, the ground state is a classical insulator. Through a first order transition at $V = V_{\mathrm{B-G}}$, a valence transition occurs to an intermediate valence (IV) gold (G) phase which is still insulating. However, under pressure the insulating gap will close for a fixed volume V_Δ. At $V = V_\Delta$, metallic conduction appears for $n_f \sim 0.8$ at a volume rather larger than the volume V_{3+} calculated for a pure trivalent configuration. Figure 1 represents the location of the different compounds at ambient pressure.

In Sm compounds, the intermediate valent state occurs between a non-magnetic $4f^6$ configuration of Sm^{2+}, with a zero angular momentum J and the Kramer's configuration

($J = \frac{5}{2}$) of Sm^{3+} ($4f^5$). It looks worthwhile to predict that, as in cerium HFC, magnetic ordering will occur when the occupancy n_f of the trivalent configuration approaches one. In this case, following the Doniach model (see [14]), the Kondo coupling should be small enough that the Kondo energy becomes smaller than the RKKY energy. However, recently it was shown by use of a microscopic hyperfine technique, nuclear forward scattering, and a macroscopic probe, ac microcalorimetry, that magnetic ordering already occurs for a rather large departure from $n_f = 1$ [15–17]. Up to $n_f \leqslant 0.8$ the 4f wavefunction seems to be renormalized to the 2+ configuration, while above $n_f \sim 0.8$ it seems linked to the 3+ configuration. Furthermore, this is related to the conduction properties: insulating below $n_f \sim 0.8$ and metallic above.

In Tm chalcogenides, the ground state of the divalent configuration ($n_f = 0$, case of TmTe) is insulating, and becomes metallic for the trivalent form. In the IVC (case of TmSe) with low n_f ($n_f \leqslant 0.8$), the many body effects of the correlation lead to the survival of an insulator. In the specific case of Tm, the novelty is that mixing occurs between two configurations with non-zero angular momentum. The divalent one (Tm^{2+} $4f^{13}$) is a Kramer's configuration with $J = \frac{7}{2}$ which leads to a doublet or a quartet crystal field ground state, while the trivalent one (Tm^{3+} $4f^{12}$) is a non-Kramer's ion with $J = 6$, which may lead to a singlet crystal field ground state. The pressure induced collapse of the insulating state is associated with a change in the magnetic structure at $p_\Delta \sim 3$ GPa [18]. Below p_Δ, i.e. for $n_f \leqslant 0.8$, the ground state is insulating, like in the low pressure intermediate valence phase of SmS and SmB_6, and antiferromagnetic, of type I, with properties basically given by a dressing towards a divalent renormalization (insulating conduction, doublet degeneracy of the local magnetic level). Above p_Δ, the ground state is metallic (like TmS, or SmS and SmB_6 at high pressure), again antiferromagnetic, but of type II, with properties renormalized to the trivalent configuration. A surprising report was that near $p \sim 6$ GPa TmSe may become insulating again [19, 20].

In this paper, we present a detailed study of the high pressure phase diagrams of TmSe, TmS and SmB_6. Since for the two first cases, specific heat is already well known for $p = 0$, and also interplay occurs between pressure and ligand effects, those compounds allow us to verify the feasibility and difficulties of high pressure microcalorimetry experiments. As TmSe is already magnetically ordered at ambient pressure, up to 3 GPa, one may expect a signal in the ac calorimetry equivalent to ambient pressure. Above 3 GPa, the signal may change as the signal may be normalized to the 3+ configuration as in TmS. Special attention is given on the pressure range around 6 GPa. The evolution of $T_N(p)$ of TmSe above 3 GPa will be compared to the nearly trivalent TmS. In SmB_6, we found evidence for a magnetically ordered ground state for $p > 8$ GPa. However, a homogeneous ground state appears only above 10 GPa.

The paper is organized as follows. First we will discuss details of the ac calorimetry technique. Then, the experimental results on TmSe, TmS and SmB_6 will be presented and an experimental conclusion will be given. In the last part, the influence of the valence on the appearance of magnetic order will be discussed in detail and a comparison to the well known high pressure phase diagrams of Ce and Yb Kondo lattice will be given.

2. Experimental details

The TmSe and TmS single crystals were prepared by Holtzberg in the IBM research centre, New York, and samples of the same batch have been intensively studied previously in CNRS Grenoble [21]. SmB_6 single crystals were grown in CEA Grenoble, out of an aluminium flux. The samples studied were cleaved to be approximately $200 \times 100 \times 50$ μm^3 in size. The high pressure experiments were performed in a diamond anvil pressure cell (see figure 2). Argon is used as a pressure transmitter. The pressure is measured at low temperature by the shift of the

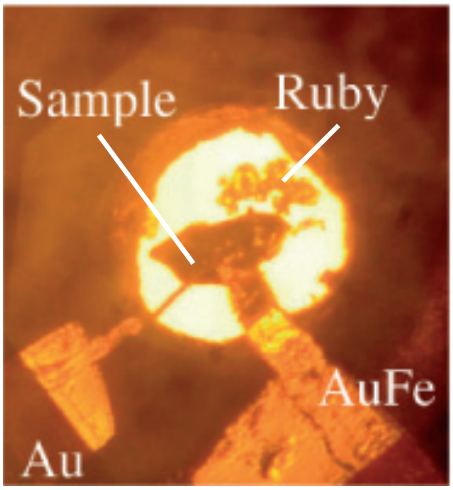

Figure 2. Zoom on the high pressure cell. A thermocouple made of Au and AuFe is welded on the sample. Argon is used as pressure medium. The pressure is measured due to the fluorescence shift of ruby. The diameter of the hole is about 350 μm.

ruby fluorescence line. In the ac calorimetry, a laser is used as heater. The beam is modulated using a mechanical chopper which works in the frequency range 50 Hz $< f <$ 5000 Hz. The temperature oscillations of the sample are measured with a Au/AuFe (0.07%) thermocouple which is spot welded on the sample. In the case of TmSe, it was glued with very diluted General Electric varnish. It is important that the thermocouple is welded at one point to avoid contributions of the thermoelectric power of the sample itself. A lock-in amplifier is used to measure the voltage of the thermocouple.

The measurements were performed in a ^{4}He bath cryostat specially adapted to change the pressure *in situ* [22, 23].

This experimental situation can be described by a first order model neglecting all internal time constants between sample, heater and thermometer [24]: $T_{\mathrm{ac}} = \frac{P_0}{\kappa + \mathrm{i}\omega C}$, where T_{ac} is the amplitude of the temperature oscillation, P_0 the average power transmitted, κ the thermal conductivity to the bath and C the specific heat. Even if the leak κ is unknown, the phase measured by the lock-in is supposed to give the possibility to extract the value of the specific heat. $C = \frac{P_0 S}{V\omega}\sin(\phi - \phi_0)$, where V is the voltage of the thermocouple, S its relative thermopower and $(\phi - \phi_0)$ the phase of the signal. If we want to minimize the importance of the phase correction, the choice of the frequency is crucial, as it balances the importance of the specific heat compared to the leak in the signal measured. From this point of view (without considering noise problems due to a decrease of the signal at high frequency), the frequency should be the highest possible. However, the experiment will show that this model is no longer valid at higher frequencies. If the frequency is too high, the sample decouples from the thermocouple and the thermocouple can be directly excited by the laser and measure only its own temperature at high frequency [25]. The next step is to include a thermal conductivity κ_{S} between the sample and the thermocouple and to consider that a small proportion a of the power is directly received on the thermocouple. In this situation (see figure 3), T_{ac} can be re-estimated [30]: $T_{\mathrm{ac}} = \frac{P_0.(1-\frac{\kappa_{\mathrm{eff}}}{\kappa_{\mathrm{S}}})}{\kappa_{\mathrm{eff}}} \frac{1+\mathrm{i}\omega a\frac{C}{\kappa_{\mathrm{S}}}}{1+\mathrm{i}\omega\frac{C}{\kappa_{\mathrm{eff}}}}$ with $\kappa_{\mathrm{eff}} = \frac{\kappa\kappa_{\mathrm{S}}}{\kappa+\kappa_{\mathrm{S}}}$ representing the total parallel thermal conductivity of the leak. Three different limits can be distinguished.

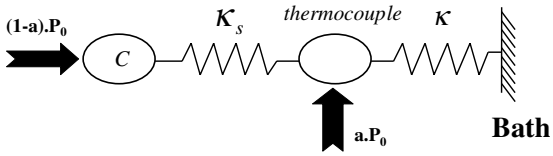

Figure 3. Schematic view of the thermal system in the pressure cell. The laser gives the power aP_0 and $(1-a)P_0$ respectively to the thermocouple and the sample.

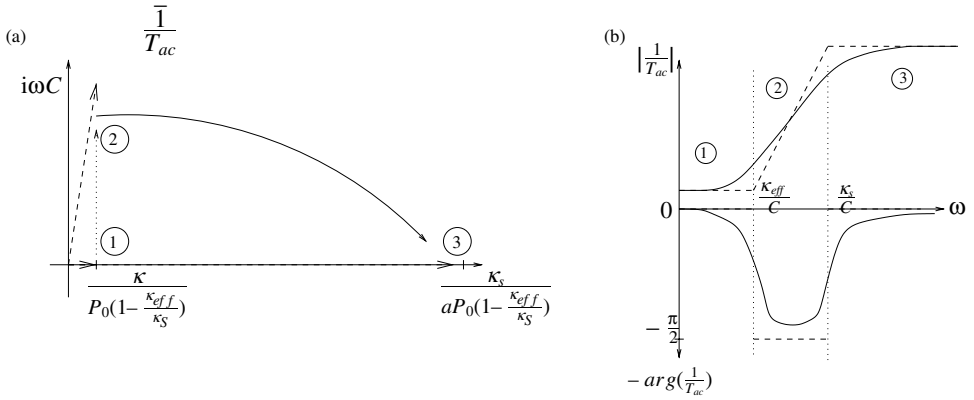

Figure 4. Part (a) shows graphically the inverse of T_{ac} in the complex representation. The leak phenomenon is on the real axis whereas capacitive effects are on the imaginary axis. The three limit cases are (1) capacitive effect is negligible and the power P_0 is transmitted to the bath with the leak κ, (2) capacitive effect becomes dominant and the component ωC is added and (3) the sample is decoupled from the thermocouple. The power received is only the fraction aP_0 and the main leak is still κ_S, towards the sample. In part (b), the schematic shape of the phase and the modulus of $\frac{1}{T_{ac}}$ is deduced from the evolution drawn in part (a). The vertical dashed lines show the cut-off frequencies $\frac{\kappa_{eff}}{C}$ and $\frac{\kappa_S}{C}$ which indicate the change of regime corresponding to (1), (2) and (3).

- At low frequency, if $\omega C \ll \kappa_{eff}$ then $T_{ac} = \frac{P_0(1-\frac{\kappa_{eff}}{\kappa_S})}{\kappa_{eff}}$. The value of the basic model is recovered: the phase of the signal is nearly zero and the inverse of the modulus is small.
- For the intermediate regime $\kappa_{eff} \ll \omega C \ll \kappa_S$ we also recover the basic model $T_{ac} = \frac{P_0(1-\frac{\kappa_{eff}}{\kappa_S})}{\kappa_{eff}+i\omega C}$. In good conditions, if frequency becomes high enough compared to the leak, the phase reaches nearly $-\frac{\Pi}{2}$.
- Finally, at high frequency, for $\kappa_S \ll \omega C$, $T_{ac} = (1-\frac{\kappa_{eff}}{\kappa_S})\frac{aP_0}{\kappa_S}$. The phase reaches zero and the modulus decreases again. Physically, the thermocouple is decoupled from the sample.

To view more clearly the frequency dependence of the system, let us consider the complex number $\frac{1}{T_{ac}}$. The phase measured by the lock-in is directly the opposite of the phase of this complex number, and the signal $\frac{1}{V}$ is directly linked to the modulus of this complex number. Part (a) of figure 4 explains the different regimes depending on the frequency. From that picture, we can roughly draw the shape of the phase and of the inverse of the modulus (see part (b) of figure 4).

Moreover, if we consider the variable change $\omega \leftrightarrow \omega C$, the shape of the dependence in ω of the argument and modulus of $\frac{1}{T_{ac}}$ (figure 4(b)) can be expanded to the dependence in ωC. Then, considering a jump in the specific heat C at the magnetic transition, the phase will be changed differently at high and low frequency. Around $\omega = \frac{\kappa_{eff}}{C}$ the signal in the phase will be

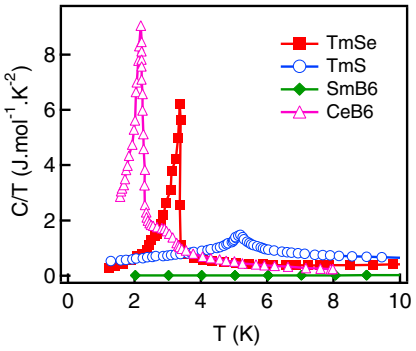

Figure 5. Specific heat divided by temperature measured at ambient pressure for TmSe [26], TmS [27], SmB_6 (measured on our sample) and CeB_6 [28].

a negative peak, but around $\omega = \frac{\kappa_S}{C}$ the signal of the phase can be a positive peak. This will be confirmed later by the experimental results.

Thus, the best frequency for the measurement is between these two cut-off frequencies. Typically, the best frequency was about 90 Hz for TmSe, 800 Hz for TmS and 4500 Hz for SmB_6. Assuming that the specific heat of TmSe is higher than that of TmS which is higher than that of SmB_6 (at least at low pressure as indicated in figure 5), this supports the model since in the conditions of measure $C\omega$ stays roughly constant.

Nevertheless, even if the behaviour of the phase is understood, the incertitude on the reference phase ϕ_0 and the complex influence of pressure keep the situation delicate. Therefore, in the following, we will usually estimate the specific heat via the simplest expression: $C = \frac{P_0 S}{V\omega}$.

The main point of the apparatus is the possibility to change the pressure at low temperature and also to use a excellent hydrostatic medium (Ar or He). To improve the feasibility of the difficult microcalorimetric measurement under hydrostatic pressure, the choice has been made to minimize the number of electrical leads and thus to use a laser as heater. The advantage of the technique is to give the pressure variation of the Néel temperature with great accuracy, i.e. a large set of pressures. Although this is an excellent method to determine the phase diagram, the difficulty is to extract the specific heat in absolute units.

3. Results

3.1. Preliminary results

Before discussing the specific heat under pressure, we present the specific heat at ambient pressure for the different systems in figure 5. The behaviour of C for the two Tm compounds is quite different. For TmSe, the specific heat has a sharp anomaly at T_N [26]. TmS is metallic and the crystal field ground state may be a singlet. Here, large fluctuations are already observed above T_N [27]. In the other case, as SmB_6 is non-magnetic we have reported here the results for CeB_6 [28] in order to have an idea of the amplitude of the signal under pressure. The comparison is worthwhile as both ($4f^1$) Ce^{3+} and ($4f^5$) Sm^{3+} are Kramer's ions with the same angular momentum $J = \frac{5}{2}$ with a lifting of the degeneracy by the crystal field in a Γ_7 doublet and a Γ_8 quartet. The successive transitions observed for CeB_6 are now well understood by a cascade from paramagnetism to quadrupolar ordering at $T_{N_1} \sim 2.9$ K and to dipolar ordering at $T_{N_2} \sim 2.2$ K, the crystal field ground state being a Γ_8 quartet [29].

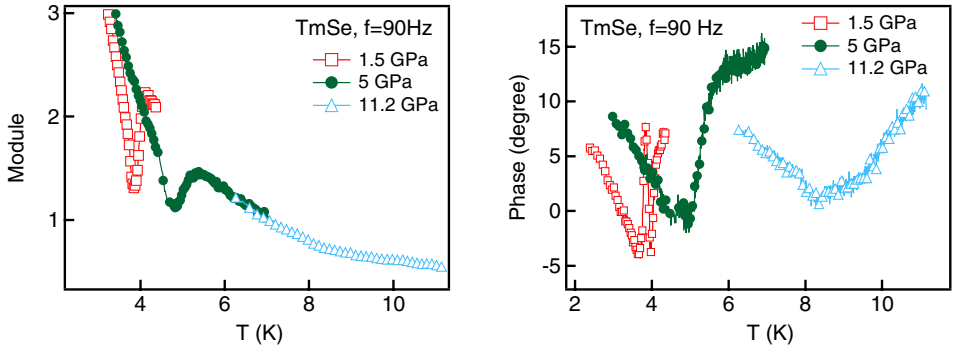

Figure 6. Raw data measured for TmSe, for several pressures (1.5, 5 and 11.2 GPa). Modulus data are normalized at high temperature; therefore, the three curves look continuous after the anomaly.

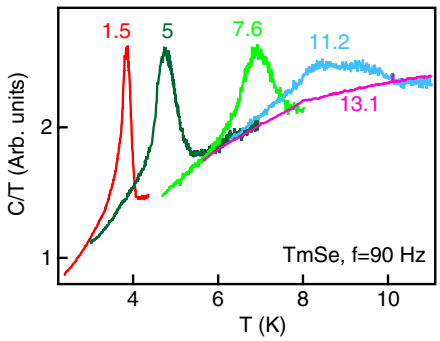

Figure 7. Evolution of the specific heat anomaly of TmSe under pressure. Data are normalized at high temperature and plotted for 1.5, 5, 7.6, 11.2 and 13.1 GPa.

3.2. TmSe

The temperature dependence of the specific heat of TmSe has been measured in a wide pressure range (1–14 GPa). Raw data are plotted in figure 6 for different pressures. The modulus and also the phase show a clear anomaly at the magnetic transition. The measurement has been realized at low frequency, so that the magnetic anomaly is seen in the phase as a negative peak. A second very sharp positive peak is also observed, inside the first negative peak, especially at low pressure. A simulation [30] shows that the huge value of the specific heat jump in TmSe can induce this second positive peak changing from the regime of low ωC to the one of high ωC. Nevertheless, the strongly negative peak of the phase shows that we are in the low frequency regime where phase correction is supposed to be used. Moreover, as the signal is huge on the modulus, the phase correction is not significant (this is explained because close to $-\frac{\Pi}{2}$ the sine function is not really sensitive). Thus we present here the simplest estimation of the specific heat $C = \frac{P_0 S}{V\omega}$. Some of the calculated curves are plotted in figure 7.

A first observation is that the magnetic anomaly is very well defined, so that the Néel temperatures can be easily extracted. To define T_N we choose the maximum of the anomaly. Furthermore, we found an unexpected broadening of the anomaly as the pressure increases. This appears below 10 GPa, when hydrostaticity is still very good (<0.1 GPa of variation in the cell) [31]. This broadening cannot be explained by pressure inhomogeneities as $\frac{dT_N}{dp}$ is small.

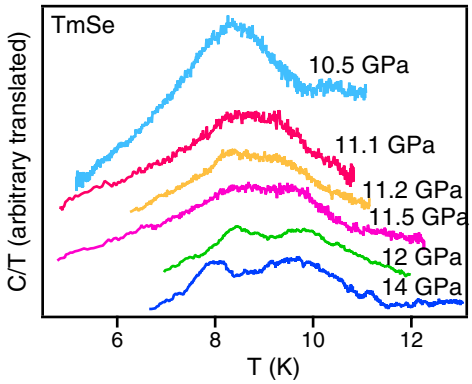

Figure 8. Observation of the splitting of the specific heat anomaly of TmSe at high pressure.

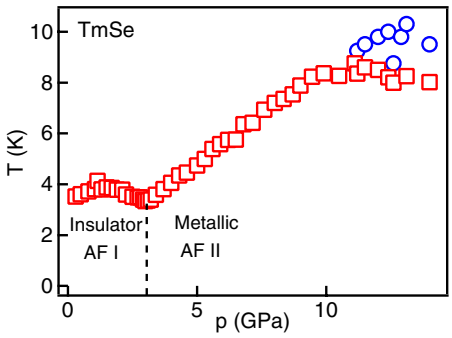

Figure 9. (p, T) phase diagram of TmSe. The squares represent the maximum of each specific heat anomaly, and the circles indicate the second maximum observed at high pressures. The dashed line show the phase transition corresponding to the slope change.

Figure 8 shows $\frac{C}{T}$ for pressures above 10 GPa. The data indicate a splitting of the magnetic anomaly, which can be followed under pressure.

The resulting phase diagram is then represented in figure 9.

The phase diagram can be distinguished in three parts. At low pressures, the evolution of T_N is quite flat and a maximum can be seen around 1.3 GPa. Then, a break in the slope around 3 GPa corresponds to the pressure of transition from the insulating AF1 phase to the metallic AF2 phase. The second magnetic structure is characterized by a linear increase of the Néel temperature with pressure.

At low pressure, our data are completely consistent with previous resistivity measurements [18–20]. The important observation is the continuous increase of T_N with pressure at high pressure. Contrary to recent resistivity measurements which showed a discontinuity in the Néel temperature around 6 GPa [32], no anomaly in $T_N(p)$ is seen in our data. Actually, our observation is consistent with a release of the 5d electrons near 3 GPa. Recent neutron measurements [32] confirm this idea as no change in the magnetic structure is found at 6 GPa. Finally, an interesting splitting of the magnetic anomaly is observed at high pressure, above 10 GPa. The evolution of the signal shape was detailed in figure 8. The origin of this splitting and the new phase is not clear. This observation pushes us to study TmS, which can be seen as a high pressure analogue of TmSe. In TmS, evidence has been reported for two different magnetic phases [33] around 5 GPa.

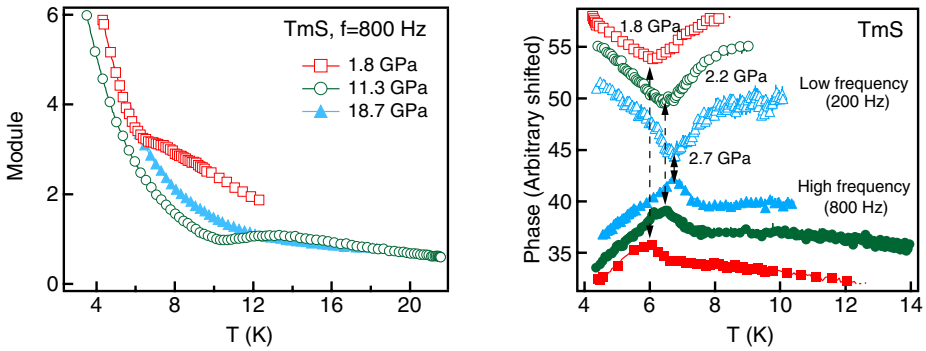

Figure 10. Raw data measured for TmS. The modulus has been drawn for 1.8, 11.3 and 18.7 GPa. The signal has been followed until very high pressure, but at the end it disappears as the curve at 18.7 GPa shows. Then, the behaviour of the phase has been detailed: the measurements at low frequency (200 Hz) and high frequency (800 Hz) have been compared and followed with pressure from 1.8 to 2.7 GPa. For the picture the phase has been arbitrarily shifted.

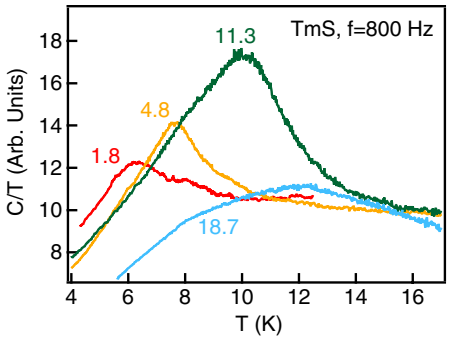

Figure 11. Evolution of the magnetic anomaly of TmS under pressure; specific heat divided by temperature has been normalized at high temperature and plotted for different pressures: 1.8, 4.8, 11.3 and 18.7 GPa.

3.3. TmS

The specific heat of TmS was measured up to 19 GPa. Raw data are plotted for several pressures in figure 10. The behaviour of the phase is detailed for the low pressures. The previous explanation is confirmed: we can observe two different regimes for the phase, depending on whether the measurement is performed at low or high frequency. This is really reproducible and stable with pressure change. This confirms that the feature occurring on the phase is very useful to detect the magnetic transition. Unfortunately, in the low frequency regime, the feature on the modulus is very small and does not allow us to extract a good shape of the specific heat. On the other hand, figure 10 shows that the modulus measured at high frequency is more clear. Even if the first order model is valid only at low frequency, figure 4(b) shows that the evolution of the modulus is still monotonic even after the first cut-off. Thus, in order to avoid a correction with an arbitrary phase ϕ_0, we prefer to show the estimation at zero order of the specific heat at 800 Hz. Some selected pressures are shown in figure 11.

Increasing the pressure, the maximum is shifted to higher temperature, from 6 to 12 K. Until 15 GPa the signal is only slightly broadened, and still very clear, but at higher pressure the signal decreases. The phase diagram of TmS is shown in figure 12. Anomalies found in

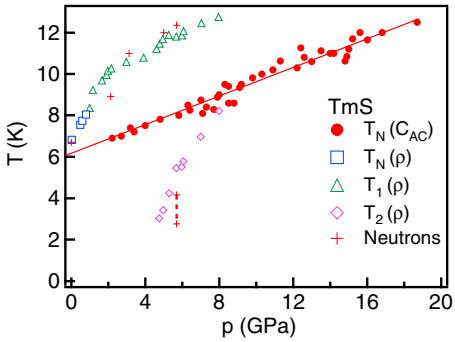

Figure 12. Phase diagram of the compound TmS; the maximum of the magnetic anomaly measured under pressure has been plotted (full circles) at the same time as previous neutron scattering [32] (crosses) and resistivity measurements [33] (empty symbols).

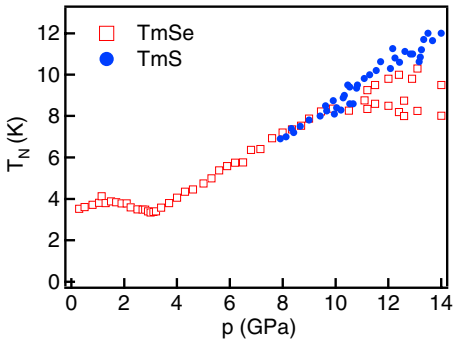

Figure 13. Combination of the phase diagram of both TmSe and TmS. For the abscissa axis, we have chosen a typical volume linked to the pressure in the TmSe compound. This means that pressure for TmS has been renormalized.

previous resistivity measurements [33] and neutron scattering [32] have also been plotted. T_1 and T_2 are kinks observed in the resistivity curve. T_1 looks linked to T_N and T_2 indicates a new phase which has also been evidenced by neutron scattering. Our study indicates a linear p increase of the Néel temperature. This observation differs from published results obtained by resistivity or neutron scattering experiments. The sensitivity of TmS to defects is well known. At ambient pressure, the value of T_N is sample dependent and varies between 5.2 and 7.05 K [34, 27]. Our sample comes from the same batch as the crystal measured in [27], where excellent agreement was found between different methods in the T_N determination.

The second anomaly below T_N observed by neutron scattering in the p range above 5 GPa is due to a 'lock-in' transition from an incommensurate to a commensurate structure. Therefore, if entropy is just slightly changed, it might be not detected by our specific heat measurement. Of course, an open question is again here the reproducibility of this second anomaly with the defects' content.

In order to compare these results to TmSe, we have scaled the pressure applied on TmS into an equivalent pressure applied on TmSe, to obtain the same volume. The pressure range has been shifted by 7 GPa, corresponding to the value where TmSe is more or less trivalent, and then normalized by the ratio of the compressibility of the two compounds (1.5×10^{-6} bar^{-1} for TmS and 3.5×10^{-6} bar^{-1} for TmSe from [35, 36]). The resulting phase diagram is plotted in figure 13.

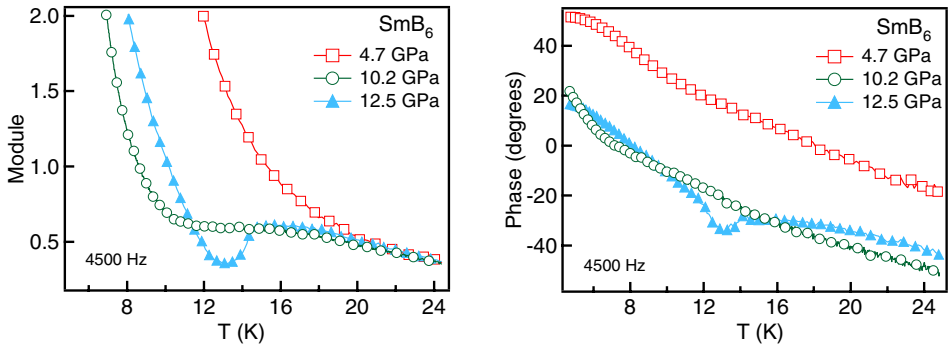

Figure 14. Raw data measured for SmB_6 for several pressures (4.7, 10.2 and 12.5 GPa). Modulus data are normalized at high temperature.

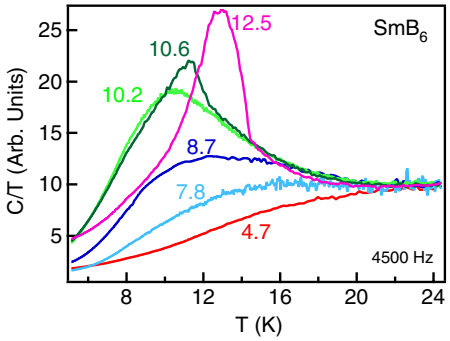

Figure 15. Growth of the magnetic anomaly of SmB_6 under pressure; specific heat divided by temperature has been normalized at high temperature and plotted for different pressures: 4.7, 7.8, 8.7, 10.2, 10.6 and 12.5 GPa.

T_N of TmS scales very well to TmSe. Of course, the points of TmSe do not follow completely the same alignment at too high pressure: the TmSe measurements themselves have to be renormalized at very high pressure as the compressibility of TmSe decreases [35, 36].

3.4. SmB_6

Finally, similar experiments have been performed for SmB_6. Long range magnetic ordering has been found above 8 GPa [17]. The features observed on the raw data are already clear. They have been plotted in figure 14 and the magnetic anomaly shows up clearly in the modulus. The feature in the modulus is huge, and we never reach the 'high frequency regime' with inversion of the phase, even for the highest frequency allowed by the set-up. Thermal contact between the sample and the thermocouple was very good. Therefore, the specific heat has been extracted only from the modulus measured at very high frequency, and a selection of the results have been plotted in figure 15. With increasing pressure, the anomaly gets more and more pronounced. In contrast to the case of TmSe, the peak gets sharper, even above 10 GPa.

The phase diagram of SmB_6 is shown in figure 16. We chose as criterion for T_N the maximum of the anomaly in $\frac{C}{T}$. In order to look more carefully at the change of the shape of the signal, we have also investigated the broadening of the anomaly which is plotted in figure 16 too.

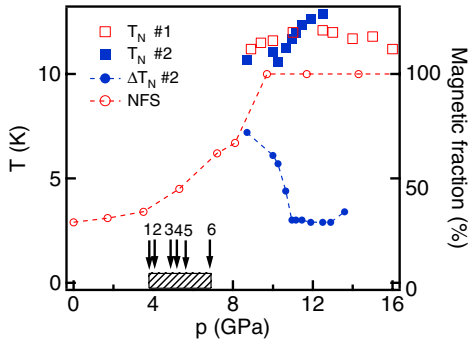

Figure 16. Phase diagram of SmB_6. The Néel temperature (dark square) and the broadening ΔT_N have been plotted in Kelvin (the broadening is the width of the anomaly peak at half the height). We have also plotted T_N for another cell measured previously (light square). These results are compared to the magnetic fraction measured by NFS [17]. The vanishing of the gap is also represented by arrows corresponding to different studies: 1—sample given by Flachbart measured in the laboratory, 2— [37], 3— [38], 4— [39], 5—sample grown by Lapertot and measured in the laboratory—and 6— [40]. The dashed box shows the wide pressure range corresponding to the collapse of the hybridization gap observed in different samples.

The evolution of the broadening shows that the anomaly peak is first very broad and then sharper. Moreover, a change of regime appears around 10 GPa. This change is significant as we can observe a clear change in the slope of the broadening i.e. roughly at the pressure where 100% of magnetic sites has been detected by NFS [17].

3.5. Experimental conclusion

It has been shown that the experimental set-up of the cell is critical to obtain correct shapes of the specific heat. In particular, the link between the thermocouple and the sample must be very good. The main incertitude concerns the knowledge of the reference phase ϕ_0. With that information, it could be possible to correct the variation due to the leak but non-monotonic behaviour of the phase before 4 K (certainly due to a T dependence of $\kappa(T)$) has discouraged us from associating ϕ_0 with the phase measured at low temperature, so the extraction of an absolute value of the specific heat remains difficult, and as the phase correction is generally small we have preferred to show here estimation derived only from the modulus. Nevertheless, the method is very useful to detect the pressure induced phase transitions (here, long range magnetism), and the *in situ* pressure generation gives a fine pressure tuning. Thus this technique is well adapted to draw phase diagrams.

The main experimental problem is to understand the broadening and the loss of the magnetic anomaly under pressure. One could imagine that the thermal contact between the sample and the thermocouple is one of the issue. But, as the systems were well welded, we do not believe in a loss of the contact. Another consideration is the behaviour of the thermal leak, as it can become huge at high pressure. The first phenomenon responsible is the argon conductivity; if we extrapolate some conductivity measurements made at higher temperature [41], the conductivity increases by more than a factor of 10 between 1 and 10 GPa. At 1 GPa, the two terms ωC and κ can already be estimated to be of the same order (10^{-3} W K^{-1}), so that a factor of 10 will be a huge effect for the relative signal measured at 10 GPa. Of course this does not explain the relatively sudden character of the effect as κ increases roughly linearly. If we consider the big compressibility of the argon [42] we can expect a reduction of the volume of the pressure chamber of the order of 30%. In this case, if

you consider the geometry of the chamber (see figure 2), a possible contact could occur between the sample and the gasket at high pressure; this could imply a big thermal contact, and a sudden increase of the thermal leak. In the case of TmSe the anomaly is lost quickly (before 10 GPa), but for other compounds the set-up allows us to follow the magnetic anomaly correctly until around 15 GPa.

For SmB_6, the situation is completely different as the broadening occurs at low pressure. There are two possible explanations for the broadening of the magnetic anomaly. First, if we assume a very sharp transition (as it seems to be, since T_N nearly jumps from zero to its maximum value), the broadening could be the effect of the pressure inhomogeneity, as even a small pressure gradient would imply a large average of the Néel temperatures. Nevertheless, to explain the experiment, one has to assume a quite big inhomogeneity, of the order of 1 GPa. Typical deviation is about only 0.1 GPa [31]. Therefore, a sound explanation is to consider the observed broadening as the signature of an intrinsic phenomenon which may be a mixed state linked to a first order transition. The system becomes homogeneous and reaches a full long range magnetic ordering only at high pressure. This idea is consistent with NFS measurements which evidence a coexistence of two phases between 5 and 10 GPa.

4. Discussion

There are different approaches for the description of magnetism of TmSe and SmB_6; but, in order to make a comparison between Tm and Sm, and even with the case of Ce and Yb, we will assume that each integer valent configuration is associated with a Kondo lattice temperature T_{KL} and that it is the comparison of this characteristic energy with other energy scales like the crystal field splitting or the magnetic intersite interaction which will lead to the renormalization towards a given configuration.

The basic idea [43] is that, compared to a single impurity, due to the release of an itinerant electron related to the valence mixing, a feedback occurs between the Kondo effect and the number of itinerant electrons. In analogy to the theoretical results known for the Kondo effect of the cerium ion in the $\frac{1}{N_f}$ expansion [44], we will assume that for the 3+ configuration $T_K^{3+} = (1 - n_f)N_f\Delta_0$, where n_f is the occupation number of the trivalent state, N_f the degeneracy ($N_f = 2J + 1$) and Δ_0 the width of the virtual 4f level in the Anderson lattice related to the density of states of the light conduction electron ($N(E_f)$) and to the hybridization mixing potential (V_{df}): $\Delta_0 = \pi V_{df}^2 N(E_f)$. Of course Δ_0 must be very sensitive to the spatial extension of the 4f orbits. One can note that the usual Kondo formula of the susceptibility χ will be recovered for the cerium case as it will correspond to $\chi^{3+} n_f$ i.e. to $T_K = \frac{T_K^{3+}}{n_f}$.

In the so called f^1–f^2 model (instead of the f^0–f^1 model suitable for the cerium electron case, and for the Kondo hole analogue ytterbium), there are theoretical studies on TmSe [43, 45–49], for Tm impurity, with n_f going from zero (f^1) to one (f^2). Basically, the large $\frac{1}{N_f}$ theory leads to very similar physics to that of the f^0–f^1 model with, however, a maxima of the Kondo temperature around $n_f \sim 1.7$. A discussion of the Kondo effect on Sm ions can be found in [50]. For the cerium case, T_K will continuously increase as n_f decreases. Yb HFCs are often viewed as the hole analogue ($4f^{13}$ configuration for Yb^{3+}) of the Ce HFC with a decrease of T_K under pressure. The Tm compounds are always magnetically ordered as the exchange energy always exceeds T_K, either by Tm^{2+} or by Tm^{3+}.

Our physical picture stresses the role of the valence mixing and the release of the 5d electron. This is the key point concerning the magnetic ground state but also the electronic ground state. This pushes us to extend the Kondo temperature formula to the lattice where the virtual bound width Δ_0 is now directly related to the bare bandwidth D of the 5d light conduction electrons: $\Delta_0 = \alpha D$, with D depending on n_f and α typically of the order of 10^{-2}

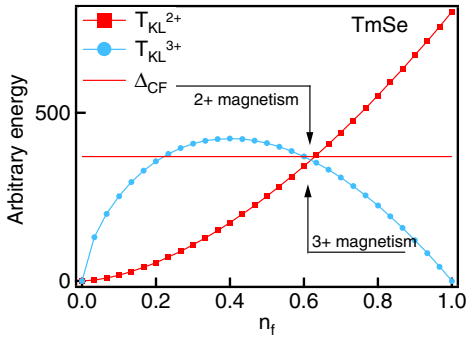

Figure 17. Comparison of the Kondo lattice temperature and the crystal field splitting in arbitrary units, in the case of TmSe, for both the 2+ and the 3+ configuration. With the criteria chosen, long range magnetism is allowed if T_{KL} is smaller than Δ_{CF}.

in order to recover a narrow virtual bound state for the impurity. The change of the number of carriers will give here $D(n_f) = D_0 n_f^{\frac{2}{3}}$.

If we apply this rule to TmSe, the Kondo temperature T_{KL} of the trivalent and divalent configurations in a lattice will be

- $T_{KL}^{3+} = \alpha D_0 (1 - n_f) n_f^{\frac{2}{3}} N_f^{3+}$
- $T_{KL}^{2+} = \alpha D_0 n_f^{\frac{5}{3}} N_f^{2+}$

where the degeneracies N_f^{3+} and N_f^{2+} are respectively 13 and 8. Figure 17 represents the Kondo temperature for the two configurations. A typical value of the overall crystal field splitting Δ_{CF} has been added to the plot. Of course, a crucial point has been to choose the ratio between Δ_{CF} and D_0 to compare Δ_{CF} with T_{KL}. In order to have a coherent behaviour, we put $\frac{\alpha D_0}{\Delta_{CF}} \sim 4$, which corresponds to a very small effective bandwidth. Anyway, if we assume that $\Delta_{CF} \sim 100$ K [26], αD_0 can be nearly of the order of magnitude of 400 K. The different energies have been traced versus n_f, varying in the same way as the pressure. If there is an extra effect as a electron gap, a simple way would be to add an extra pressure dependence on D ($D = 0$ for $p < p_\Delta$).

Extrapolating from the numerous studies performed on Ce HFC, the occurrence of long range magnetism requires at least the recovery of usual rare earth properties, notably the full reaction to the crystal field splitting i.e. $k_B T_{KL} < \Delta_{CF}$. Of course a main consideration is the relative strength of the intersite exchange interaction and T_{KL} as discussed for the usual Doniach model [14, 51, 52]. Long range magnetism will occur only if the energy scale of the coupling is stronger than the Kondo energy. Nevertheless, in our simple view, we compare only Δ_{CF} and T_{KL}. Therefore, we only indicate when long range magnetism will be possible. For each configuration, long range magnetism will be possible while T_{KL} is smaller than Δ_{CF}; this means we assume the coupling is already strong enough. Of course, the positions of the intersections are very sensitive to the ratio $\frac{\Delta_{CF}}{\alpha D_0}$. Nevertheless, this basic model explains qualitatively the general shape of the phase diagram. At low pressure, n_f is small, and long range magnetism is due to Tm^{2+}; then at higher pressure, when n_f increases, this long range magnetism disappears and long range magnetism due to Tm^{3+} appears. The change of regime observed at 3 GPa is well reproduced. At this critical pressure, a critical value of n_f is reached, where the renormalization of the wavefunction changes from the 2+ to the 3+ ground state since the Kondo effect becomes crucial for the Tm^{2+} ions and is not strong enough for Tm^{3+}.

For the Sm Kondo lattice, the previous formula of T_{KL}^{3+} is plotted in figure 18. Now, $\frac{\alpha D_0}{\Delta_{CF}} \sim 2$ is chosen. The interpretation is the same: a magnetic ground state is possible when its

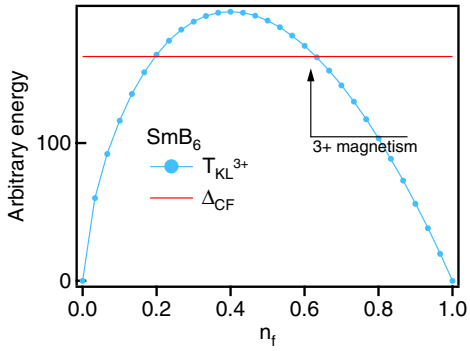

Figure 18. Comparison of the Kondo lattice temperature and the crystal field splitting in arbitrary units, for the 3+ configuration. In the case of SmB_6 as only the trivalent state is magnetic, long range magnetism will be allowed if T_{KL}^{3+} becomes smaller than Δ_{CF}.

trivalent Kondo lattice temperature (dominating the long range magnetism here, since Sm^{2+} is non-magnetic) is low enough compared to a crystal field energy. At low value of n_f the long range magnetism will disappear as the exchange energy will drop.

The important point is that T_{KL}^{3+} reaches a broad maximum near $n_f = 0.4$. This is a critical difference from the cerium case, which corresponds to the release of the 4f electron from the 4f shell: $Ce^{3+} \Longleftrightarrow Ce^{4+} + 5d$. If no extra electron is considered, one may find that T_{KL}^{3+} goes, in the Ce case, as $T_{KL}^{3+} = (1 - n_f)^{\frac{5}{3}} \alpha D_0 N_f$ (with $N_f = 2J + 1 = 6$). By contrast to the previous case, T_{KL}^{3+} never reaches a maximum in the Ce case. Actually, this naive scheme gives the correct result that in Ce HFC T_K decreases continuously with increasing n_f.

In these considerations, the width of the virtual bound state is weak; the motion of the spin dynamics of the trivalent configuration appears slow even for $n_f \sim 0.8$ as observed in SmS, SmB_6 by NFS or in $YbRh_2Si_2$ [53]. This may suggest that the 4f–5d correlation is a favourable factor to slow down the valence fluctuation. This consideration leads us to propose that SmB_6, like SmS, can be regarded in the low pressure gold phase ($p < p_\Delta$) as an excitonic dielectric semiconductor with the electron promoted from f shells spread over the p orbitals of neighbouring boron sites but with the same symmetry as the f electron in the central Sm site [54, 55]. An alternative idea is that the electron (5d) created by the mixing of the 4f state and the hole produced in the conduction band screen the 4f hole and form a bound state in a low carrier density medium [56]. Up to now, there is no consideration of the pressure dependence of the 5d screening and thus of the disappearance of the reported many body effects. In terms of a Kondo approach, one may think that one way to describe the extra many body effect is to consider the possibility of the Kondo effect of the 5d electron itself. A many body treatment will be required, so long as its T_K (5d) is lower than its crystal field splitting Δ_{CF} (5d). Of course, T_K (5d) will be far greater than T_K (4f), but also Δ_{CF} (5d) $> \Delta_{CF}$ (4f). A change will occur under pressure since in all reported cases (Sm^{3+}, Yb^{3+}, Tm^{3+}) their T_K (4f) decrease under p while T_K (5d) increase with pressure. When T_K (5d) $> \Delta_{CF}$ (5d) there will be no more reason to consider the extra many body effects of the 5d electron, which could be considered then as dissolved in the Fermi sea.

In the case of TmSe, entering in the trivalent state, there are two reasons that the physics will be dominated by the formation of a magnetic moment on an initial singlet ground state: the Kondo effect and a probable singlet crystal field level. As pointed out, the two mechanisms leads to rather similar increases of the sublattice magnetization under pressure on increasing the intersite exchange coupling. Thus the difference in the crystal field ground state limits the

comparison of TmSe with SmB_6 and SmS. However, let us emphasize the similarity: up to $n_f \sim 0.8$, the physics appear renormalized to the divalent configuration, not only governing the magnetic properties, but also the electronic properties (formation of many body insulating state); above $n_f \sim 0.8$ the physics is now governed by the trivalent configuration (metallic conduction and nature of the magnetic order parameter).

Microscopic evidence for the 2+ configuration in SmS, SmB_6 and even TmSe was given by inelastic neutron scattering experiments and measurement of the magnetic form factor [57, 58]. The demonstration of a dressing towards the 3+ configuration for SmS and SmB_6 was done by NFS as both the quadrupolar and dipolar magnetic hyperfine structure are characteristic of a 3+ state even for $n_f \sim 0.8$. Macroscopically, suggestions of the 2+ renormalization of TmSe at $p = 0$ come from the specific heat, and of the 3+ renormalization of TmSe above 3 GPa from its continuity with the quasitrivalent compound TmS.

Concerning SmS and SmB_6 we have to be careful of the coincidence in the appearance of long range magnetism and closing of the hybridization gap. For SmS, the coincidence has been found. An extrapolation made from inelastic measurement on $Sm_{0.83}Y_{0.17}S$ suggests strongly that Sm–Sm exchange interactions play a major role even in the low pressure gold phase [58]. No similar influence is observed for SmB_6 certainly due to the isolation of the Sm ion with the B cage. The gap is closed as function of pressure before long range magnetic ordering appears. Typically, the gap is closed between 4 and 6 GPa [37, 39, 38, 40], but long range magnetism does not appear before 8 GPa and a homogeneous magnetic phase picture without phase separation may occur only above 10 GPa.

The difference between SmB_6 and SmS is not so surprising, as their band structures are completely different due to symmetries which are different. Local spin density approximations (LSDA + U approach) have been published for Sm monochalcogenides [59] and SmB_6 [60]. For SmS, NaCl type crystal structure with the space group $Fm3m$, the occupation number n_f is found equal to 0.55 (valence $v = 2.55$) in the low pressure gold phase; a non-zero magnetic moment is always obtained. For SmB_6, CaB_6 type crystal structure with the space group $Pn3m$, the calculations always produce an integer valence ground state, either divalent or trivalent. A small hybridization energy gap is recovered in SmB_6 for samarium in the divalent state. It was emphasized that the magnetism of golden SmS as well as the formation of the IV state in SmB_6 requires us to go beyond this mean field approximation.

Finally, by comparison to results on Ce intermetallic heavy fermion compounds, in these Sm and Tm systems, a long range magnetism characteristic of the trivalent configuration occurs far below the pressure where the trivalent state will be reached. This phenomenon is quite similar to that observed in $YbRh_2Si_2$. Physically, the interesting fact is that, here, the Kondo temperature of the trivalent configuration (and also of the divalent one for the Tm case) never grows very high. Furthermore, due to to the stronger localization of the 4f shell than in the Ce case [61], the width of the virtual bound state Δ_0 in Sm, Tm and Yb examples is far lower than the corresponding width for the Ce impurity. Δ_0 may often be comparable to Δ_{CF}, the overall spin splitting, while for the Ce case Δ_0 may be at least one order of magnitude higher than Δ_{CF} with the spin orbit coupling comparable to Δ_0.

5. Conclusion

Ac calorimetry with *in situ* p variation at low temperature is a powerful technique to define without ambiguity the magnetic phase diagram under pressure. We hope that our experimental report may help experimental progress.

The common point in the three investigated systems TmSe, SmB_6, and SmS [16, 15] is the link between the electric conduction and the renormalization to divalent or trivalent configurations at low temperature. Looking more deeply at SmS and SmB_6, a main difference

appears between the clear onset of long range magnetism at p_Δ in SmS and the large pressure window in SmB_6 (6 GPa $< p <$ 10 GPa), where an inhomogeneous behaviour is observed. A homogeneous magnetic phase occurs in SmB_6 only above 10 GPa. It is amazing to observe that if $p_\Delta = 2$ GPa is remarkably reproducible in SmS [16] a large dispersion appears for SmB_6 (around 3 GPa). The next step is to understand the role of the disorder in SmB_6 and the impact on the collapse of the gap and the appearance of long range magnetism.

Acknowledgment

We would like to thank Christophe Marcenat for his precious clarification in the explanation of the phase behaviour of ac microcalorimetry measurements.

References

[1] Flouquet J 2005 *Prog. Low Temp. Phys.* vol XV, ed W Halperin (Amsterdam: Elsevier)
[2] Trovarelli O, Geibel C, Mederle S, Langhammer C, Grosche F M, Gegenwart P, Lang M, Sparn G and Steglich F 2000 *Phys. Rev. Lett.* **85** 626–9
[3] Plessel J, Abd-Elmeguid M M, Sanchez J P, Knebel G, Geibel C, Trovarelli O and Steglich F 2003 *Phys. Rev.* B **67** 180403
[4] Wachter P 1994 *Handbook of Physics and Chemistry of Rare Earths* ed K A Gschneider *et al* (Amsterdam: North-Holland)
[5] Malterre D 1996 *Adv. Phys.* **45** 299
[6] Launois H, Rawiso M, Holland-Moritz E, Pott R and Wohlleben D 1980 *Phys. Rev. Lett.* **44** 1271
[7] Haen P, Lapierre F, Mignot J M, Kappler J P, Krill G and Ravet M F 1985 *J. Magn. Magn. Mater.* **47/48** 490
[8] Wertheim G K, Eib W, Kaldis E and Campagna M 1980 *Phys. Rev.* B **22** 6240
[9] Brewer W D, Kalkowski G, Kaindl G and Holtzberg F 1985 *Phys. Rev.* B **32** 3676
[10] Beaurepaire E, Kappler J P and Krill G 1990 *Phys. Rev.* B **41** 6768
[11] Röhler J *et al* 1982 *Valence Instabilities* ed P Wachter and H Boppart (Amsterdam: North-Holland) p 215
[12] Dallera C, Annese E, Rueff J-P, Grioni M, Vanko G, Braicovich L, Barla A, Sanchez J-P, Gusmeroli R, Palenzona A, Degiorgi L and Lapertot G 2005 *J. Phys.: Condens. Matter* **17** S849
[13] Ogita N, Nagai S, Udagawa M, Iga F, Sera M, Oguchi T, Akimitsu J and Kunii S 2005 *Physica* B **359–361** 941
[14] Doniach S 1977 *Physica* B **91** 231
[15] Barla A, Sanchez J P, Haga Y, Lapertot G, Doyle B P, Leupold O, Ruffer R, Abd-Elmeguid M M, Lengsdorf R and Flouquet J 2004 *Phys. Rev. Lett.* **92** 066401
[16] Haga Y, Derr J, Barla A, Salce B, Lapertot G, Sheikin I, Matsubayashi K, Sato N K and Flouquet J 2004 *Phys. Rev.* B **70** 220406
[17] Barla A, Derr J, Sanchez J P, Salce B, Lapertot G, Doyle B P, Ruffer R, Lengsdorf R, Abd-Elmeguid M M and Flouquet J 2005 *Phys. Rev. Lett.* **94** 166401
[18] Ribault M, Flouquet J, Haen P, Lapierre F, Mignot J M and Holtzberg F 1980 *Phys. Rev. Lett.* **45** 1295
[19] Ohashi M, Takeshita N, Mitamura H, Matsumura T, Suzuki T, Goto T, Ishimoto H and Môri N 1999 *Physica* B **259–261** 326–8
[20] Ohashi M, Takeshita N, Mitamura H, Matsumura T, Suzuki T, Mori T, Goto T, Ishimoto H and Môri N 2001 *J. Magn. Magn. Mater.* **226–230** 158–60
[21] Holtzberg F, Flouquet J, Haen P, Lapierre F, Lassailly Y and Vettier C 1985 *J. Appl. Phys.* **57** 3152–3
[22] Salce B, Thomasson J, Demuer A, Blanchard J J, Martinod J M, Devoile L and Guillaume A 2000 *Rev. Sci. Instrum.* **71** 2461
[23] Demuer A, Marcenat C, Thomasson J, Calemczuk R, Salce B, Lejay P, Braithwaite D and Flouquet J 2000 *J. Low Temp. Phys.* **120** 245–57
[24] Sullivan P F and Seidel G 1968 *Phys. Rev.* **173** 679–85
[25] Marcenat C and Méasson M A 2005 private communication
[26] Berton A, Chaussy J, Cornut B, Flouquet J, Odin J, Peyrard J and Holtzberg F 1981 *Phys. Rev.* B **23** 3504
[27] Berton A, Chaussy J, Flouquet J, Odin J, Peyrard J and Holtzberg F 1985 *Phys. Rev.* B **31** 4313
[28] Fujita T, Suzuki M, Komatsubara T, Kunii S, Kasuya T and Ohtsuka T 1980 *Solid State Commun.* **35** 569–72
[29] Shiina R, Sakai O, Shiba H and Thalmeier P 1998 *J. Phys. Soc. Japan* **67** 941
[30] Méasson M A 2005 *Thése de Doctorat* Université Joseph Fourrier, Grenoble

[31] Thomasson J *et al* 2004 private communication
[32] Mignot J M, Goncharenko I N, Link P, Maysumura T and Suzuki T 2000 *Hyperfine Interact.* **128** 207–24
[33] Ohashi M, Takeshita N, Mitamura H, Matsumura T, Uwatoko Y, Suzuki T, Goto T, Ishimoto H and Môri N 2000 *Physica* B **281/282** 264–6
[34] Chouteau G, Holtzberg F, Pena O, Penney T and Tournier R 1979 *J. Physique Coll.* **40** C5361
[35] Lassailly Y, Vettier C, Holtzberg F, Flouquet J, Zeyen C M E and Lapierre F 1983 *Phys. Rev.* B **28** 2880–2
[36] Batlogg B, Ott H R, Kaldis E, Thöni W and Wachter P 1979 *Phys. Rev.* B **19** 247–59
[37] Gabani S, Bauer E, Berger S, Flashbart K, Paderno Y, Paul C, Pavlík V and Shitsevalova N 2003 *Phys. Rev.* B **67** 172406
[38] Moshchalkov V V, Berman I V, Brandt N B, Pashkevich S N, Bogdanov E V, Konovalova E S and Semenov M V 1985 *J. Magn. Magn. Mater.* **47/48** 289–91
[39] Cooley J C, Aronson M C, Fisk Z and Canfield P C 1995 *Phys. Rev. Lett.* **74** 9
[40] Beille J, Maple M B, Wittig J, Fisk Z and Delong L E 1983 *Phys. Rev.* B **28** 12
[41] Tretiakov K V and Scandolo S 2004 *J. Chem. Phys.* **121** 11177–82
[42] Shimizu H, Tashiro H, Kume T and Sasaki S 2001 *Phys. Rev. Lett.* **86** 4568–71
[43] Flouquet J, Barla A, Boursier R, Derr J and Knebel G 2005 *J. Phys. Soc. Japan* **74** 178–85
[44] Hewson A C 1993 *The Kondo Problem to Heavy Fermions* (Cambridge: Cambridge University Press)
[45] Newns D M and Read N 1987 *Adv. Phys.* **36** 799–849
[46] Read N, Dharamvir K, Rasul J W and Newns D M 1986 *J. Phys. C: Solid State Phys.* **19** 1597
[47] Nunes A C, Rasul J W and Gehring G A 1986 *J. Phys. C: Solid State Phys.* **19** 1017
[48] Yafet Y, Varma C M and Jones B 1985 *Phys. Rev.* B **32** 360
[49] Saso T 1988 *J. Magn. Magn. Mater.* **76/77** 176–8
[50] Sakai O, Shimizu Y and Kasuya T 1992 *Prog. Theor. Phys.* **108** 73
[51] Benoit A, Flouquet J, Ribault M, Flouquet F, Chouteau G and Tournier R 1978 *J. Physique Lett.* **39** 94
[52] Bredl C D, Steglich F and Schotte K D 1978 *Z. Phys.* B **29** 327
[53] Sichelschmidt J, Ivanshin V A, Ferstl J, Geibel C and Steglich F 2003 *Phys. Rev. Lett.* **91** 156401
[54] Kikoin K A and Mishchenko A S 1995 *J. Phys.: Condens. Matter* **7** 307
[55] Curnoe S and Kikoin K A 2000 *Phys. Rev.* B **61** 15714
[56] Kasuya T 1994 *Europhys. Lett.* **26** 277
[57] Mignot J M and Alekseev P A 1995 *Physica* B **215** 99
[58] Alekseev P A, Mignot J-M, Ochiai A, Nefeodova E V, Sadikov I P, Clementyev E S, Lazukov V N, Braden M and Nemkovski K S 2002 *Phys. Rev.* B **65** 153201
[59] Antonov V N, Harmon B N and Yaresko A N 2002 *Phys. Rev.* B **66** 165208
[60] Antonov V N, Harmon B N and Yaresko A N 2002 *Phys. Rev.* B **66** 165209
[61] Waber J T and Cromer D T 1965 *J. Chem. Phys.* **42** 4116